Nucleic Acids Research, 2025, **53**, gkaf120
https://doi.org/10.1093/nar/gkaf120
RNA and RNA-protein complexes

Protein bL38 facilitates incorporation of uL6 during assembly of the 50S subunit in *Flavobacterium johnsoniae*

Md. Siddik Alom[1,2], Dominic Arpin[3,4], Haojun Zhu[3,4], Brenna N. Hay[5], Leonard J. Foster[5], Joaquin Ortega[3,4,*], Kurt Fredrick[1,2,6,*]

[1]Ohio State Biochemistry Program, The Ohio State University, Columbus, OH 43210, United States
[2]Center for RNA Biology, The Ohio State University, Columbus, OH 43210, United States
[3]Department of Anatomy and Cell Biology, McGill University, Montreal, Quebec H3A 0C7, Canada
[4]Centre for Structural Biology, McGill University, Montreal, Quebec H3G 0B1, Canada
[5]Department of Biochemistry and Molecular Biology, Michael Smith Laboratories, University of British Columbia, Vancouver, British Columbia, V3T1Z4, Canada
[6]Department of Microbiology, The Ohio State University, Columbus, OH 43210, United States

[*]To whom correspondence should be addressed. Tel: +1 614 292 6679; Email: fredrick.5@osu.edu
Correspondence may also be addressed to Joaquin Ortega. Tel: +1 514 398 5230; Email: joaquin.ortega@mcgill.ca

Abstract

Previous studies of the 70S ribosome from *Flavobacterium johnsoniae* revealed a novel ribosomal protein, bL38, which interacts with uL6 on the 50S subunit. This 5.6 kDa protein is conserved across the Bacteroidia and encoded downstream of bL28 and bL33 in a three-gene operon. Here, we show that bL38 is critical for the growth of *F. johnsoniae*, and depletion of bL38 leads to accumulation of immature 50S particles, which lack uL6 and retain precursor rRNA sequences. Cryo-EM analysis of these particles reveals several putative assembly intermediates, all showing an absence of electron density for uL6 and the entire uL12 stalk region and additional densities corresponding to the unprocessed ends of the pre-23S rRNA. Extra copies of the uL6 gene can rescue the phenotypes caused by bL38 depletion, suggesting that bL38 facilitates uL6 incorporation during 50S subunit biogenesis. Cryo-EM analysis of 50S particles from this rescued strain reveals nearly twice as many intermediates, suggesting a broader and more robust assembly landscape. Differential scanning fluorimetry shows that uL6 of *F. johnsoniae* is intrinsically unstable, and bL38 increases the melting temperature of uL6 by 12°C. Collectively, these data suggest that bL38 binds and stabilizes uL6, thereby promoting 50S biogenesis in the Bacteroidia.

Graphical abstract

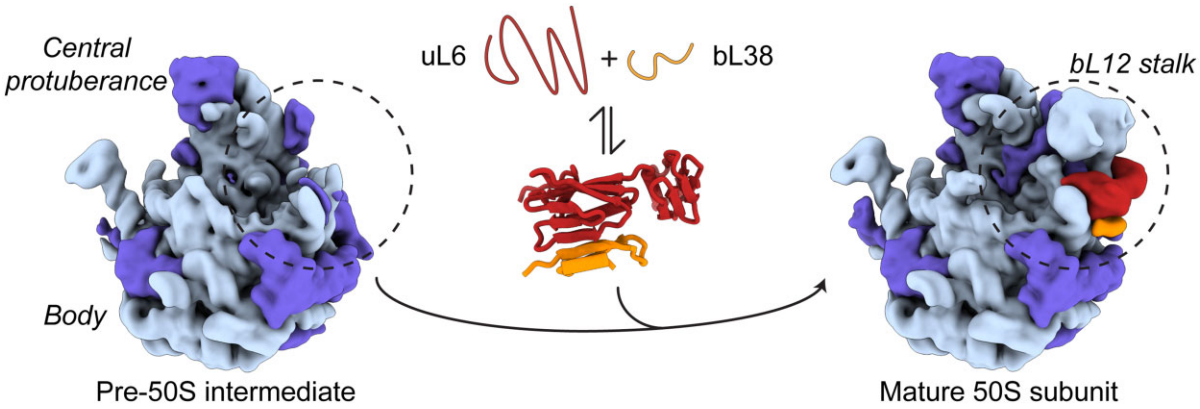

Introduction

Ribosomes are large two-subunit enzymes that catalyze protein synthesis in all cells. The bacterial 70S ribosome is composed of three large RNAs (16S rRNA, 23S rRNA, 5S rRNA) and more than 50 distinct ribosomal proteins (r-proteins). Most r-proteins make extensive contacts with rRNA, often involving positively-charged termini or loops embedded deep within rRNA folds. About two-thirds of the r-proteins are conserved across all domains of life and denoted with the prefix "u" for universal [1, 2]. The remainder are bacterial-specific and denoted with the prefix "b." Thirty-two of the former and 18 of the latter represent the core set of r-proteins,

Received: March 7, 2024. **Revised:** February 4, 2025. **Editorial Decision:** February 4, 2025. **Accepted:** February 6, 2025

present in all bacteria. Several other r-proteins (e.g. bS1, bS21, bTHX, bL25, uL30, and bL37) are variably present, depending on the lineage [1–5].

Structures of ribosomes from representatives of various bacterial phyla have now been determined. These structures reveal the remarkable similarities of conserved features of the ribosome as well as unique lineage-specific characteristics. A novel ribosomal protein, bL38, was recently identified as part of the 70S ribosome from *Flavobacterium johnsoniae* (Fig. 1), a member of the phylum Bacteroidota [6]. This 5.6 kDa protein consists of a beta hairpin packed against an alpha helix (Fig. 1B). The gene encoding bL38, *rpmL*, is ubiquitous across class Bacteroidia and lies downstream of *rpmB* (bL28) and *rpmG* (bL33). RNA-seq and ribo-seq data from *F. johnsoniae* provide strong evidence that these three genes comprise an operon [6, 7]. In the context of the 50S subunit, bL38 interacts intimately with the C-terminal domain of uL6, effectively extending one of its beta sheets by two strands (Fig. 1B). Nearly 40% of bL38's surface area buried by this interaction. Protein bL38 additionally contacts helices H95 and H97 of 23S rRNA, the former also known as the sarcin-ricin loop (SRL) (Fig. 1B). The functional role of bL38 remains unclear. *F. johnsoniae* uL6 looks much like other uL6 proteins, and the space occupied by bL38 in the *F. johnsoniae* ribosome is vacant in other bacterial ribosomes (Fig. 1C).

In this work, we interrogate the role of bL38 in *F. johnsoniae*. We show that depletion of bL38 causes inhibition of growth and accumulation of premature 50S particles, which lack uL6 and fail to form the bL12 stalk region. Overproduction of uL6 restores growth and enables subunit biogenesis in the absence of bL38. Structural analysis of 50S particles formed under these two conditions suggests that a robust 50S assembly landscape with multiple parallel pathways depends on the efficient incorporation of uL6. Differential scanning fluorimetry (DSF) indicates that purified uL6 of *F. johnsoniae* is intrinsically labile, and bL38 increases the thermostability of uL6 substantially. Collectively, our data provide strong evidence that bL38 is needed to facilitate uL6 incorporation during 50S assembly.

Material and methods

Strain construction

All strains derived from wild-type *F. johnsoniae* isolate UW101 [8]. The bL38-depletion strain SA08 was made using precise allelic replacement, essentially as described [9]. Briefly, ~1 kb regions of DNA upstream and downstream of *rpmL* were amplified separately from the *F. johnsoniae* chromosome. Using Gibson Assembly [10], these two fragments were fused to form a ~2 kb fragment lacking the coding region of *rpmL* and cloned into the erythromycin (Erm) resistant suicide vector pYT313 [11], generating pSA03. Using tri-parental mating, pSA03 was moved into *F. johnsoniae* cells harboring the covering plasmid pSA04, which contains *rpmL* downstream from an IPTG-inducible promoter in vector pCP23 [12] and confers tetracycline (Tet) resistance. Transconjugants were selected on solid casitone yeast extract (CYE) media [13] containing Tet (20 μg/mL) and Erm (100 μg/mL), and colonies were screened by PCR for integration of pSA03 into the chromosome via homologous recombination. Such recombinants were then grown overnight in liquid CYE media containing IPTG (1 mM) and lacking Erm, and cells were plated on solid CYE containing IPTG, Tet, and sucrose (5%). Sucrose-resistant colonies were screened for loss of Erm resistance, indicative of a second recombination event and plasmid pSA03 loss. These candidates were screened by PCR to identify those with *ΔrpmL*, corresponding to strain SA08.

Strain SA20 was made in the same way as SA08, except that the coding region of *rpmL* was replaced by that of *rplF* (uL6). Strain SA22 was made in the same way as SA20 except with pSA12 as the covering plasmid. Plasmid pSA12 is pSA04 carrying *rplF* under transcriptional control of its operon's native promoter and positioned downstream of *rpmL*, in the opposite orientation. Two more strains, SA28 and SA30, which lack *rpmL* entirely, were also generated. Strain SA28 was made by replacing *rpmL* with *rplF* in UW101 (with no covering plasmid). Strain SA30 was made by replacing *rpmL* with *rplF* in UW101 cells harboring pSA15, a derivative of pSA12 that lacks *rpmL*.

Growth measurements

For the bL38-depletion strains, cells were grown at 30°C overnight in CYE media containing IPTG. The following day, cells from 1 mL of culture were pelleted, washed with media lacking IPTG, and used to inoculate fresh pre-warmed media (50 mL) containing or lacking IPTG. Growth was monitored by measuring OD_{600} every 30 minutes for at least 12 hours. In parallel, growth of wild-type *F. johnsoniae* was monitored.

For the plating assay, the washed cells were serially diluted in fresh CYE, and aliquots (15 μL) were spotted onto CYE plates containing or lacking IPTG. Once the liquid of the spotted samples was fully absorbed, the plates were incubated at 30°C for two days. Tet (20 μg/mL) was often included in the media when strains harbored a tetracycline-resistant plasmid, as specified in the figure legends.

Polysome analysis

Cells were grown at 30°C in 50 mL CYE with Tet (20 μg/mL) and IPTG (1 mM). Cells were gently pelleted, washed with 50 mL CYE (no IPTG), and resuspended in 10 mL CYE. An aliquot of cell suspension was used to inoculate fresh media (50 mL; CYE + Tet), containing or lacking IPTG, pre-equilibrated at 30°C. Cultures were grown for three hours, and cells were rapidly chilled and subjected to polysome profiling analysis as described [14].

Experiments involving pulse-labeling of RNA were performed in the same way, except that [^{3}H]-uridine (50 μL; 500 μCi) was added after the wash step. Twenty-eight fractions were collected from each 11 mL gradient, and liquid scintillation was used to quantify the ^{3}H signal in each fraction.

PAGE analysis of total RNA

For each strain analyzed, an aliquot of culture (1 mL) was collected just prior to the rapid chilling step of the polysome analysis described above. Cells were pelleted and total RNA was extracted with TRIzol (Invitrogen). In parallel, total RNA from wild-type *F. johnsoniae* grown without antibiotic or inducer was extracted. Samples (250 ng) were loaded onto a 4% polyacrylamide 8M urea gel in TBE buffer (90 mM Tris-borate pH 8.0, 2 mM EDTA) and electrophoresed for 15 h at 300V. The gel was stained with SYBR Gold, visualized with Typhoon 9100 imager (Cytiva), and quantified with ImageQuant 10.2 (Cytiva) software.

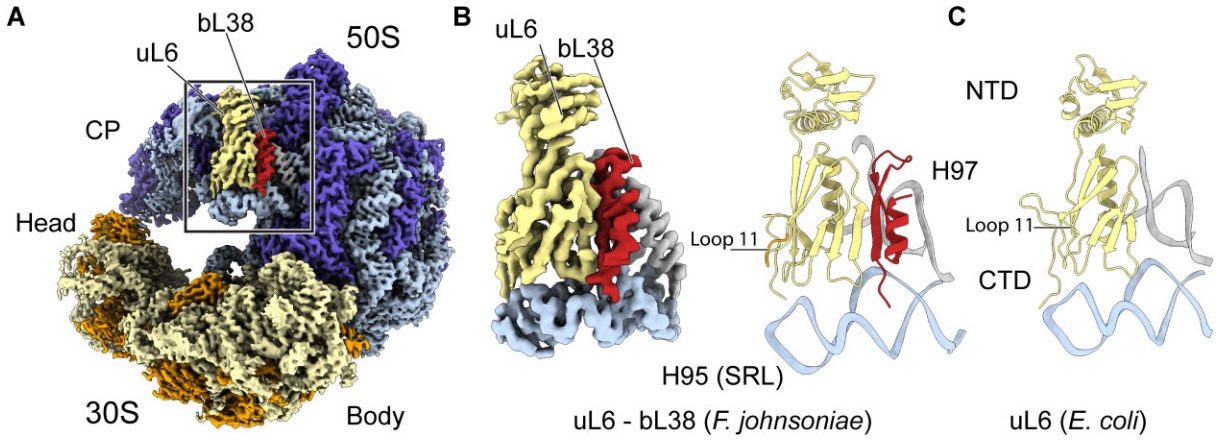

Figure 1. Novel ribosomal protein bL38. (**A**) A view of the 70S ribosome of *F. johnsoniae*, with uL6 colored pale yellow and bL38 colored red. (**B**) Close-up of the uL6-bL38 region, showing the segmented cryo-EM density on the left and ribbon representation on the right. Pale yellow, uL6; red, bL38; light blue, helix H95; grey, helix H97. (**C**) Ribbon representation of the analogous region of the *E. coli* 70S ribosome, with the same color coding. CTD, C-terminal domain; NTD, N-terminal domain. Loop 11 of both uL6 structures is indicated, with the four-residue insertion characteristic of Bacteroidia highlighted in orange. Images were made using PDB files 8G34 and 7JIL.

Primer extension analysis

A fluorescently-labeled primer (5′-Cy5-CTTTTCGCAGCT TATCACGTCC-3′; 620 ng), complementary to nucleotides 55–76 of 23S rRNA, was incubated with total RNA (750 ng) in 10 μL annealing buffer (50 mM K-HEPES pH 7.6, 100 mM KCl) for 10 min at 50°C, and then cooled to room temperature. Then, 10 μL of extension mix (130 mM Tris-HCl pH 8.5, 10 mM $MgCl_2$, 10 mM DTT, 0.44 mM each dNTP, 0.3 U AMV reverse transcriptase) was added. After a brief spin, reactions were incubated at 42°C for 1 h, and products were resolved via 6% denaturing PAGE. To map the primer extension products, the same primer was used to sequence plasmid pZM06 [15], which carries *rrnA*.

Sodium dodecyl sulphate-polyacrylamide gel electrophoresis analysis

Ribosomal particles (70 pmol) were precipitated with 15% trichloroacetic acid (TCA) at 4°C overnight. Proteins were pelleted in a microfuge by spinning at 15 000 rpm for 30 min at 4°C. Pellets were washed with acetone, dried, and resuspended in 30 μL loading buffer [65.8 mM Tris-HCl (pH 6.8), 2% sodium dodecyl sulphate (SDS), 26% (w/v) glycerol, 0.01% bromophenol blue]. Samples were heated at 95°C for 10 min, placed on ice, loaded onto a tricine-urea-SDS-polyacrylamide (15%) gel [16], and electrophoresed at 3W (constant) for 20 h. Gels were stained with Coomassie brilliant blue, and analyzed using a Typhoon 9100 instrument and ImageQuant 10.2 software (Cytiva).

Large-scale preparations of ribosomal particles

For structural studies, 50S, 70S, and polysome particles were isolated as described above, except that cells were cultured at 20 times the scale, a cryo-mill (SPEX SamplePrep) was used for cell lysis, and gradient sedimentation involved larger SW32 rotors (Beckman) for centrifugation (22K rpm for 12 h). Fractions corresponding to 50S, 70S, and polysome peaks were collected, and particles were pelleted by ultracentrifugation (33K rpm for 17 h) in a Ti-50.2 (Beckman) rotor. Pellets were rinsed and particles were dissolved in TMN buffer (50 mM Tris-HCl pH 7.5, 10 mM $MgCl_2$, 100 mM NH_4Cl, and 6 mM β-mercaptoethanol). Aliquots were flash frozen and stored at −80°C.

Mass spectrometry

Ribosomal particles (100 pmol) were TCA precipitated as described above. Pellets were resuspended and proteins resolved by Sodium dodecylsulphate-polyacrylamide gel electrophoresis (SDS-PAGE) in preparation for in-gel digestion as described [17]. Disulfide bonds were reduced with tris(2-carboxyethyl)phosphine and alkylated with chloroacetamide. Samples were digested with 0.5 μg trypsin/LysC (Promega V5071) at a ratio of 1:50 trypsin/LysC:protein overnight at 37°C, followed by a second trypsin/LysC spike-in at a ratio of 1:200 trypsin/LysC:protein for an additional 4 h. Peptides were desalted and purified using C18 STAGE-tips as described [18]. Samples were reconstituted in 0.1% formic acid and 0.5% acetonitrile. Concentrations were determined with a NanoDrop One (Thermo Scientific) using the A205 Scope method (absorbance at 205 nm, baseline correction at 340 nm) and 75 ng were injected and separated on-line using NanoElute UHPLC system (Bruker Daltonics) with Aurora Series Gen2 (CSI) analytical column. Peptides were analyzed with a Trapped Ion Mobility-Time of Flight mass spectrometer (TimsTOF Pro2; Bruker Daltonics) with Parallel Accumulation-Serial Fragmentation scan mode for DDA acquisition. The data were searched on MaxQuant (version 1.6.8.0) using label-free quantification at a peptide and protein FDR of 1% against the *F. johnsoniae* UniProt database (UP000006694). The proteomics data have been deposited to the ProteomeXchange Consortium via the PRIDE [19] partner repository with the dataset identifier PXD050205.

Cryo-electron microscopy

To prepare the grids containing 50S particles from SA08(-IPTG) cells and 50S particles and 70S ribosomes from SA22(-IPTG) cells, we prepared a dilution of these particles at a concentration of 160, 180, and 70 nM, respectively, in TMN buffer. These solutions were centrifuged at 12 100 × g for 5 min at 4°C to remove any aggregates, and the supernatants were used for grid preparation.

The sample containing the polysome fraction from the SA22(-IPTG) strain was treated with RNase I before applying it to the cryo-EM grids. To this end, RNase I (Thermo Scientific, EN0601) and SUPERase IN (Invitrogen, AM2696) were pre-diluted to 1 U/μL with TMN buffer. A volume of 2 μL of 5 μM polysome sample was first diluted with 16 μL of TMN buffer to assemble the nuclease reaction. Subsequently, we added 1 U of RNase I and incubated for 30 min on ice before the reaction was quenched by 1 U of SUPERase IN. The sample was then further diluted to 70 nM before being applied to cryo-M grids.

We used cryo-EM grids (c-flat CF-2/1–3Cu-T). Before the samples were applied, the grids were prepared by evaporating a continuous layer of carbon (5–10 nm) to reduce exposure of the ribosomal particles to the air-water interface. Immediately before applying the samples, grids were washed in chloroform overnight and treated with a negative glow discharge in air at 5 mA for 15 s. Grids with samples applied were vitrified in liquid ethane using a Vitrobot Mark IV (Thermo Fisher Scientific Inc.). We used a blotting force of + 1 or + 3 for 3 s. The Vitrobot chamber was set to 25°C and 100% relative humidity. All datasets were collected at FEMR-McGill using a Titan Krios microscope operated at 300 kV and equipped with a Gatan BioQuantum LS K3 direct electron detector. The software used for data collection was SerialEM [20]. Images were collected in counting mode at a nominal magnification of 105 000×, producing images with a calibrated pixel size of 0.855 Å. Movies for all datasets were collected using 30 frames with a total dose of 50 $e^-/Å^2$ except for the polysome sample, where movies were collected with 40 frames and a total dose of 40 $e^-/Å^2$.

Image processing

All image processing steps were done using CryoSPARC v4 [21]. Cryo-EM movies were corrected for beam-induced motion using Patch Motion Correction with default settings that included information up to 5Å resolution when aligning frames, a B-factor 500 and a 0.5 calibrated smoothing constant applied to the trajectories. All frames in the movies were used to produce the merged micrograph. CTF parameter estimation was done using Patch CTF Estimation using default settings in the program. The minimum and maximum resolution considered to estimate the CTF parameters were 25 and 4 Å. The minimum and maximum defocus values were set at 1000 and 40 000 Å. Images with a CTF fit resolution of 3 Å or better were kept for further processing.

In the dataset obtained for the 50S particles from the SA08(-IPTG) strain, particles on the selected micrographs were initially picked using Blob Picker with a circular blob and a minimum and maximum particle diameter of 150 and 250 Å on a subset of 1000 randomly selected micrographs. The maximum resolution considered in the micrographs was 20 Å. The angular sampling used was 5 degrees, and the minimum particle separation distance was 1 (in units of particle diameters). Picked particles were curated using a NCC score of 0.35 and a local power between 1200 and 1700. These particles were extracted using a box size of 400 pixels, and Fourier cropped it to 100 pixels. Particles were then subjected to 2D classification and curated to generate 2D templates. In the 2D classification step, we requested 50 classes and selected 0.85 and 0.99 as the inner and outer window radii. The maximum resolution considered in the images was 6 Å, and we used 2 Å for the initial uncertainty factor. All other parameters were kept at default settings. Template picker was then used with a diameter of 250 Å to pick particles on all movies. Particles were curated using an NCC score of 0.3 and local power between 1760 and 2487. This clean particle stack was extracted using a box size of 420 pixels and then subjected to Ab initio 3D reconstruction. For the Ab-Initio step, we selected 0.85 and 0.99 as inner and outer window radius, requested 3 classes, and set 35 and 12 Å as the minimum and maximum resolution to consider. The number of iterations before and after annealing starts and ends was set to 200 and 300, respectively, and the increase of Fourier radius at each iteration was 0.04. All other parameters for this routine were used with the default settings and values. Two subsets were found from the Ab-initio 3D reconstruction, and both were independently refined with a Homogenous refinement with default setting and C1 symmetry to generate consensus maps and initial models for refinements. A second round of Ab initio was performed on each refined subset, and particle heterogeneity was explored through 3D classification. To this end, we performed a series of 3D classifications using Simple as the initialization mode (initial models are obtained from randomly selected particle subsets) and requested four classes each time with a maximum resolution to consider of 6 Å. Resulting maps from the exhaustive 3D classification were visually inspected in Chimera [22, 23], and clusters of particles representing similar assembly intermediates were merged.

High-resolution refinements were performed in two stages: In the first step, particles from merged subsets were subjected to a Homogeneous Refinement using the initial consensus refinement cryo-EM map generated from the curated set of particles as a 3D reference (after proper scaling and filtering using a 30 Å low-pass Fourier filter). These Homogeneous Refinements were run under default settings with C1 symmetry. The resulting maps were used as the initial model for a second refinement step that consisted of a Non-Uniform Refinement run under default settings with C1 symmetry and with activated optimized per-particle defocus, optimized per-exposure group CTF parameters and options "Fit Spherical Aberration," "Fit tetrafoil." Average resolution estimation and local resolution analysis were done with cryoSPARC using the gold-standard approach [24]. Cryo-EM map visualization was performed in UCSF Chimera and Chimera X [22, 23].

The datasets collected for the 50S, 70S, and polysome particles from SA22(-IPTG) were processed using a similar strategy with a few adjustments as follows. In all three datasets, CTF parameters were estimated with a minimum and maximum resolution of 30 Å and 3 Å, respectively, and the cutoff resolution was set to 4 Å during micrograph curation. Additionally, to exclude drifted micrographs, a threshold on the total full-frame motion distance was applied to exclude drifted micrographs. For the initial particle pick using Blob Picker, the maximum particle diameter was set to 350 Å when picking 70S and polysome ribosome particles, with a minimum separation distance of 0.5–0.8 (in the unit of particle diameter). Particles were extracted with a box size of 424 or 464 pixels for the 50S or 70S/polysome ribosome particles, respectively, and further binned by 4 by Fourier cropping. The particles remained binned by 4 during 2D and 3D classifications; therefore, the maximum resolution used in the following steps before full-size reconstruction was limited to 6.84 Å. Initial templates were generated through 2D classification with an initial uncertainty factor of 1. Additional template improvement steps, with two rounds of template picking using the

existing template and an increasing number of micrographs, were conducted before picking all micrographs. After generating initial templates, all template picking jobs used 250 or 280 Å as particle diameters. Extracted particles were curated first by 2D classification and secondly by two layers of Ab initio reconstruction, as described above. The clean particle stack was then homogenously refined to build a single consensus map. Subsequently, three to four layers of 3D classification were performed to classify particles until exhaustion. To reveal small differences, such as the presence or absence of the uL6 protein, focused classification approaches were applied. The focused masks were generated through UCSF Chimera and further dilated and soft-padded by 4 pixels in CryoSPARC. In each focused 3D classification step, the initialization mode was switched to 'Input', using the previous homogeneous reconstruction as the two initial volumes. In these cases, the convergence criteria were tuned to 1% instead of 2%. Before final refinements, particles were re-extracted by a local motion correction job with a calibrated smoothing lambda set to autotune. Appropriate box sizes were used without Fourier cropping. These full-size particles were refined using Non-Uniform refinement, as mentioned above.

Purification of uL6 and bL38

The genes encoding uL6 of *Escherichia coli*, uL6 of *F. johnsoniae*, and bL38 of *F. johnsoniae* were each amplified and cloned into the overexpression vector pET24b. The resulting plasmids were transformed into *E. coli* BL21 DE3 codon plus competent cells (Stratagene) to generate the overexpression strains. Cells were grown in shaking flasks of LB medium with kanamycin (50 μg/mL) at 37°C. At OD_{600} of 0.5, cells were induced with 1 mM of isopropyl-3-D-thiogalactopyranoside (IPTG). After 2.5 or 3 h of induction (for bL38 or uL6, respectively), the cells were harvested by centrifugation. The cells were resuspended in lysis buffer [30 mM HEPES (pH 7.6), 10 mM $MgCl_2$, 50 mM NaCl, 0.1 mM phenylmethyl-sulfonyl fluoride] and lysed via French Press. Lysate was centrifuged at 18 000 RPM for 20 min in a JA-20 rotor (Beckman). Each overexpressed protein was then purified as described below.

In the case of *E. coli* uL6, the overexpressed protein was mainly found in the soluble fraction. The clarified supernatant was loaded onto a 5 mL Resource-S column (Cytiva), pre-equilibrated with buffer A (30 mM HEPES pH 7.6, 10 mM $MgCl_2$, 50 mM NaCl). The column was washed with 50 mL of buffer A, and bound protein was eluted using a linear NaCl gradient (50–1000 mM) over 10 column volumes. Fractions containing *E. coli* uL6 were identified by SDS-PAGE, pooled, and concentrated using microfiltration devices (Amicon). Samples of concentrated protein (200 μL) were loaded onto a Superdex^{TM} 75 Increase 10/300 GL column (Cytiva) equilibrated with buffer B (30 mM HEPES pH 7.6, 10 mM $MgCl_2$, 50 mM NaCl, 100 mM KCl). Fractions that contained *E. coli* uL6 were pooled, and the purified protein was concentrated, aliquoted, flash-frozen, and stored at −80°C.

In the case of *F. johnsoniae* uL6, the overexpressed protein was found in the insoluble (inclusion body) fraction. The pellet was resuspended in buffer C (30 mM HEPES pH 7.6, 6.0 M urea) to dissolve the inclusion bodies, and the sample was centrifuged at 15 000 RPM for 10 min at 4°C to remove any residual undissolved material. The clarified supernatant was loaded onto a 5 mL Resource S column (Cytiva), pre-equilibrated with buffer C. The column was washed with 50 mL of buffer C, and bound protein was eluted using a linear NaCl gradient (50–1000 mM) over 10 column volumes. Fractions containing *F. johnsoniae* uL6 were pooled and dialyzed against buffer B. The resulting renatured protein was concentrated using microfiltration devices (Amicon) and further purified using the Superdex^{TM} 75 Increase 10/300 GL column, as described above.

In the case of *F. johnsoniae* bL38, the overexpressed protein was mainly found in the soluble fraction. The protein was purified using the same two-column method described above for *E. coli* uL6.

Differential scanning fluorimetry

DSF was performed using SYPRO Orange (Sigma Aldrich), essentially as described [25, 26]. Proteins in buffer B (20 μL), alone or in combination (as specified in legends), were mixed with SYPRO Orange (final concentration 10x, as defined by the manufacturer) and distributed into wells of thin-walled microtiter plates (BioRad). Thermal denaturation was performed using a CFX96 RT-qPCR instrument (Bio-Rad). Temperature was increased from 10°C to 95°C, at 1°C per cycle increments, with an 8 s equilibration time for each temperature.

Results

Protein bL38 is critical for growth of F. johnsoniae

Our initial attempts to delete *rpmL* were unsuccessful. So, we engineered a bL38-depletion strain, SA08, which lacks *rpmL* on the chromosome but carries a plasmid-borne copy of *rpmL* downstream from an IPTG-inducible promoter (Table 1). We found that growth of SA08 is dependent on IPTG, based on plating and culturing assays (Fig. 2, Table 1). These results indicate that bL38 is critical for growth of *F. johnsoniae*.

Depletion of bL38 causes an accumulation of subunit particles

Next, we began to assess the effects of bL38 depletion on ribosomes in the cell. SA08 cells were grown to mid-log phase in the presence of IPTG, washed, resuspended in fresh media with or without IPTG, and allowed to grow for another three hours. Cells were harvested and their lysates were fractionated via sucrose gradient sedimentation (Fig. 3A–C). In cells depleted of bL38 (-IPTG), increased levels of subunit particles and decreased levels of 70S ribosomes and polysomes were observed. In fact, the subunit (30S and 50S) peaks accounted for half of the total ribosomal particles in the cell (Fig. 3B). These data are consistent with a ribosome biogenesis defect preventing subunits from entering the translationally active pool.

Evidence that bL38 depletion blocks 50S biogenesis

In principle, the large 30S and 50S peaks of Fig. 3B could represent stalled assembly intermediates, active subunits without functional partners, and/or degradation intermediates. To help distinguish these possibilities, we repeated the sucrose gradient sedimentation experiment described above except with ^{3}H-uridine in the fresh media to label the newly-synthesized RNA. Fig. 3D and E compares the profiles of total (A_{254}) and newly formed (^{3}H-labeled) RNA across the gradient. In the control (+IPTG) case, the ^{3}H signal across the

Table 1. Doubling times of various strains

Strain	Chromosomal mutations	Plasmid-borne ribosomal genes	Copies of *rplF*	Experient 1[a]		Experiment 2[b]	
				+IPTG	-IPTG	+IPTG	-IPTG
UW101	none	NA	1	ND	67 ± 1	ND	65 ± 1
SA08	*ΔrpmL*	*rpmL* (bL38)	1	78 ± 1	>250	68 ± 1	183 ± 8
SA20	*ΔrpmL::rplF*	*rpmL* (bL38)	2	76 ± 1	157 ± 5	64 ± 1	116 ± 1
SA22	*ΔrpmL::rplF*	*rpmL* (bL38), *rplF* (uL6)	3[c]	75 ± 1	108 ± 1	66 ± 1	93 ± 2
SA28	*ΔrpmL::rplF*	NA	2	ND	ND	ND	117 ± 1
SA30	*ΔrpmL::rplF*	*rplF* (uL6)	3[a]	ND	ND	ND	104 ± 1

Data represent doubling times in minutes, mean ± SEM ($n \geq 3$). NA, not applicable. ND, not determined.
[a]Tetracycline included in all cases but UW101.
[b]Tetracycline excluded.
[c]Two on the chromosome and one on a multi-copy plasmid.

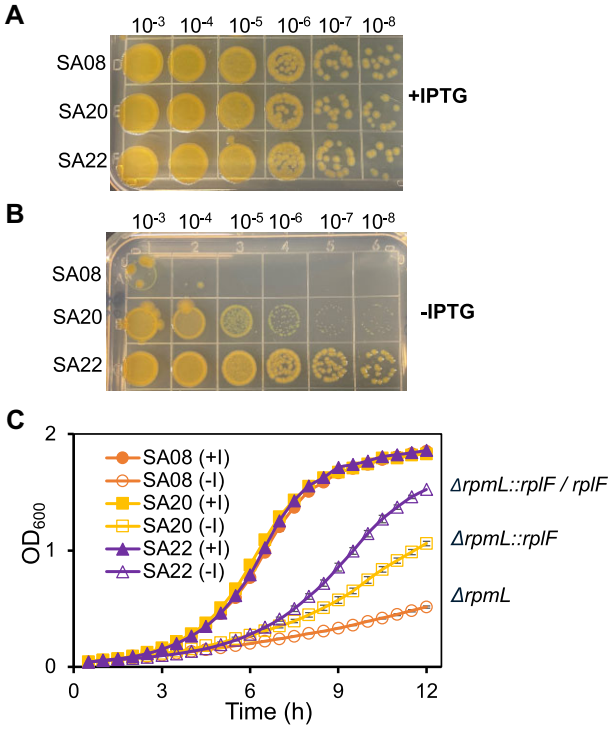

Figure 2. Growth of bL38-depletion strains of *F. johnsoniae*. (**A–C**) Analyzed are bL38-depletion strains, which lack *rpmL* (bL38) on the chromosome but contain a plasmid-borne copy of *rpmL* downstream from an IPTG-inducible promoter. Strains SA08, SA20, and SA22 are analogous except that the latter two carry additional copies of the uL6 gene (*rplF*). (**A** and **B**) Cell suspensions were diluted and spotted onto CYE + Tet plates containing or lacking IPTG, as indicated. Plates were incubated at 30°C for 48 h and then photographed. (**C**) Washed cells of SA08, SA20, and SA22 were used to inoculate fresh CYE + Tet media containing or lacking IPTG, as indicated, and growth at 30°C was monitored by optical density at 600 nm (OD_{600}). Shown are results of three independent experiments, where data points and error bars correspond to mean ± SEM values.

gradient roughly follows the A_{254} signal (Fig. 3D). By contrast, in the -IPTG case, a large ^3H signal is seen specifically in the 50S fraction, consistent with the accumulation of inactive pre-50S particles in the absence of bL38 (Fig. 3E). Considerably lower ^3H signal is seen in the 30S region, despite the high A_{254} peak, implying that newly formed 30S subunits are active, compete well with recycled subunits, and make their way into the 70S and polysome fractions. The excess of free 30S subunits, indicated by the large A_{254} peak, likely results from a shortage of active 50S subunit partners (Fig. 3D and E).

Depletion of bL38 causes accumulation of precursor 23S rRNAs

It is well known that ribosome assembly and rRNA processing go hand in hand [27]. To investigate whether bL38 depletion influences rRNA processing, we extracted total RNA from WT cells and SA08 cells grown for 3 h in the presence or absence of IPTG and analyzed the RNA in two ways. First, we used denaturing PAGE (4%) with SYBR Gold staining to resolve and detect the major RNA species (Fig. 4A). In the WT case, bands corresponding to mature 16S and 23S rRNA were predominant. In the SA08(-IPTG) case, a smear of larger RNAs, presumably corresponding to precursor 23S (pre-23S) rRNA molecules, was seen above the 23S rRNA band. Another band, migrating between 16S and 23S rRNA, was also evident. These species were also seen in the SA08(+IPTG) case, albeit at lower abundance. Second, we used primer extension to evaluate 5′ end processing of 23S rRNA (Fig. 4B, Supplementary Fig. S3). In the WT case, most of the cDNA corresponds to the mature 5′ end. Two longer cDNA products were also observed, corresponding to pre-23S intermediates with 5′ nucleotides U-117 and G-195. In the SA08(-IPTG) case, these pre-23S species were much more abundant, and additional precursor and/or degradation intermediates were also seen (Fig. 4B). These primer extension data confirm that the slow-migrating RNAs of Fig. 4A represent pre-23S molecules. In the SA08(+IPTG) case, the proportion of mature 23S rRNA was considerably higher than in the SA08(-IPTG) case but not as high as in the WT case. For both analyses, bands corresponding to pre-23S and 23S rRNA were quantified, and the percentage of mature rRNA was calculated in all cases (Fig. 4C). Compared to WT (>95% maturation), the bL38-depletion strain exhibited a clear defect in 23S rRNA processing in the absence of IPTG (30–40% maturation), which is mostly reversed in the presence of IPTG (~70% maturation).

Protein uL6 is underrepresented in 50S particles from cells depleted of bL38

From WT cells and SA08 cells grown with or without IPTG, we isolated 50S particles and analyzed their protein composition. Using one-dimensional tricine SDS-PAGE (Fig. 5), we could resolve many r-proteins and found that two were largely

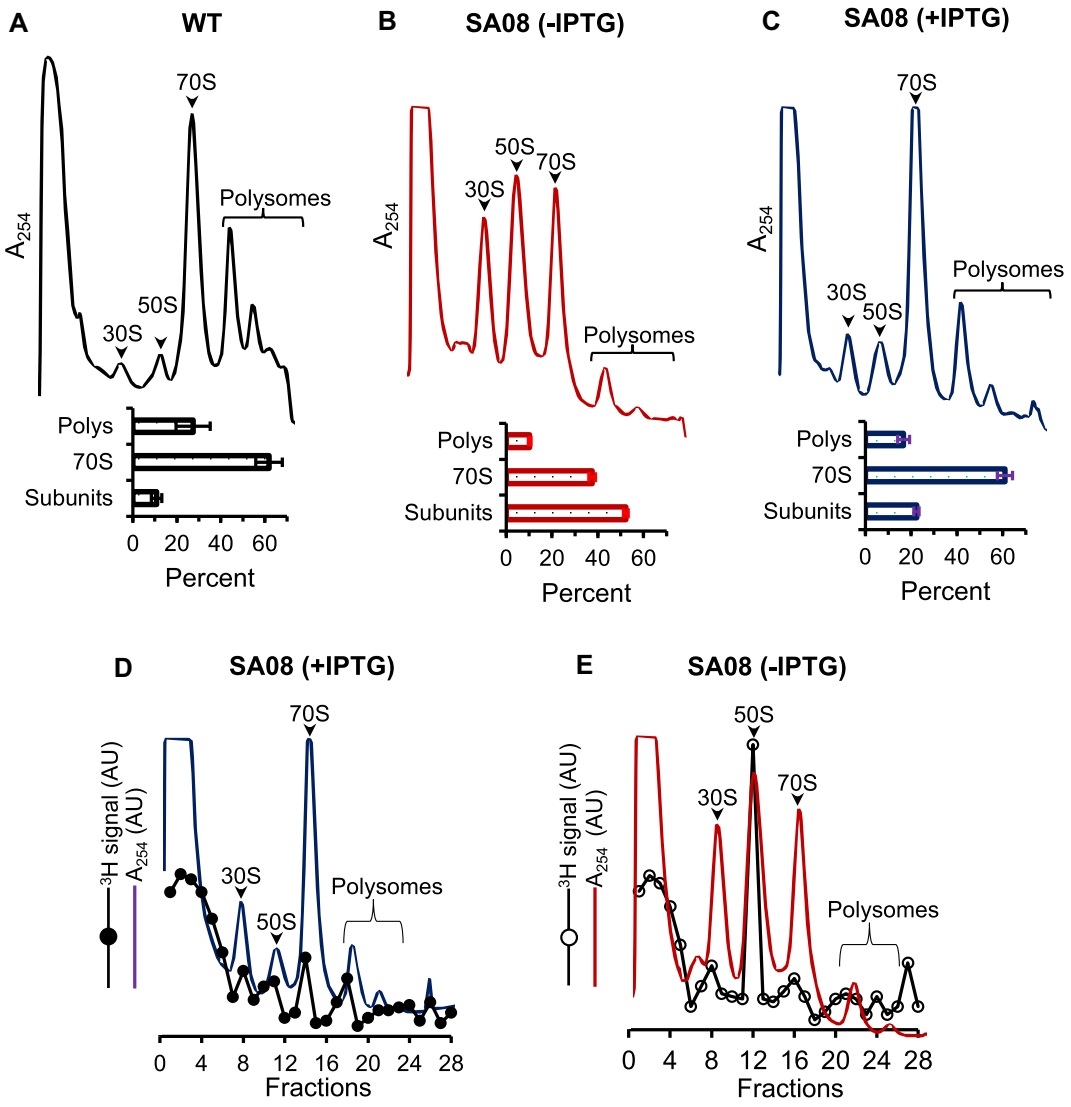

Figure 3. Depletion of bL38 results in accumulation of pre-50S particles. Representative sucrose gradient profiles of wildtype *F. johnsoniae* (**A**), strain SA08 grown without IPTG (**B**), and stain SA08 grown with IPTG (**C**). Absorbance (A_{254}) peaks corresponding to 30S, 50S, 70S, and polysomes are indicated. Histograms below show the proportion of polysomes, 70S ribosomes, and subunits (30S plus 50S), determined by integration of the A_{254} peaks. Data represent the mean ± SEM ($n = 3$). (D and E) Evidence that pre-50S particles accumulate upon depletion of bL38. SA08 cells in mid-logarithmic phase were washed and resuspended in media containing ^{3}H-uridine and containing (**D**) or lacking (**E**) IPTG, cultured for 3 h, and subjected to sucrose gradient analysis. Shown are measures of total RNA (A_{254}) and labeled RNA (^{3}H signal) across each gradient. AU, arbitrary units.

absent in the SA08(-IPTG) case. Corresponding bands from WT subunits were excised, and LC-MS/MS analysis confirmed that uL6 and bL38 are the underrepresented proteins. Densitometry scans of individual lanes suggest stoichiometries of ~0.3 for uL6 and ~0.01 for bL38, respectively, in 50S particles from the SA08(-IPTG) cells (Fig. 5B). Next, we used label-free-quantification (LFQ) LC-MS/MS to gain a more comprehensive view of the protein composition of 50S particles from SA08(-IPTG) and SA08(+IPTG) cells (Supplementary Fig. S2, Supplementary Table S1). These data suggest that a handful of proteins, including uL6, uL10, and bL38, are underrepresented in SA08(-IPTG) particles. Protein uL10 lies near uL6 and forms part of the bL12 stalk. We also performed the LFQ analysis on 70S ribosomes from the same cells and found that levels of uL6 and uL10 were fully restored while the level of bL38 was partially restored. These data suggest that subunits lacking uL6 and/or uL10 cannot enter the actively translating pool.

Cryo-EM analysis of 50S particles formed in the absence of bL38

The large 50S peak from SA08(-IPTG) cells was collected, and these particles were analyzed by cryo-EM. Image classification approaches found that this sample contained a mixture of ribosomal particles at various stages of assembly (Fig. 6). A cryo-EM map was obtained for each assembly intermediate, and the maps were refined to a resolution ranging from 2.6 to 3.5 Å (Supplementary Figs S3 and S4; Supplementary Table S2). Overall, these assembly intermediates could be divided into two main groups. The first group, comprised of classes 1–3, is characterized by the absence of density for rRNA elements and r-proteins of the central protuberance (CP). The second group includes larger particles that show at least part of the CP (classes 4–6) and mature subunits (class M).

Class 1 was the least mature intermediate, accounting for 3% of the population. In class 1 particles, the solvent side of

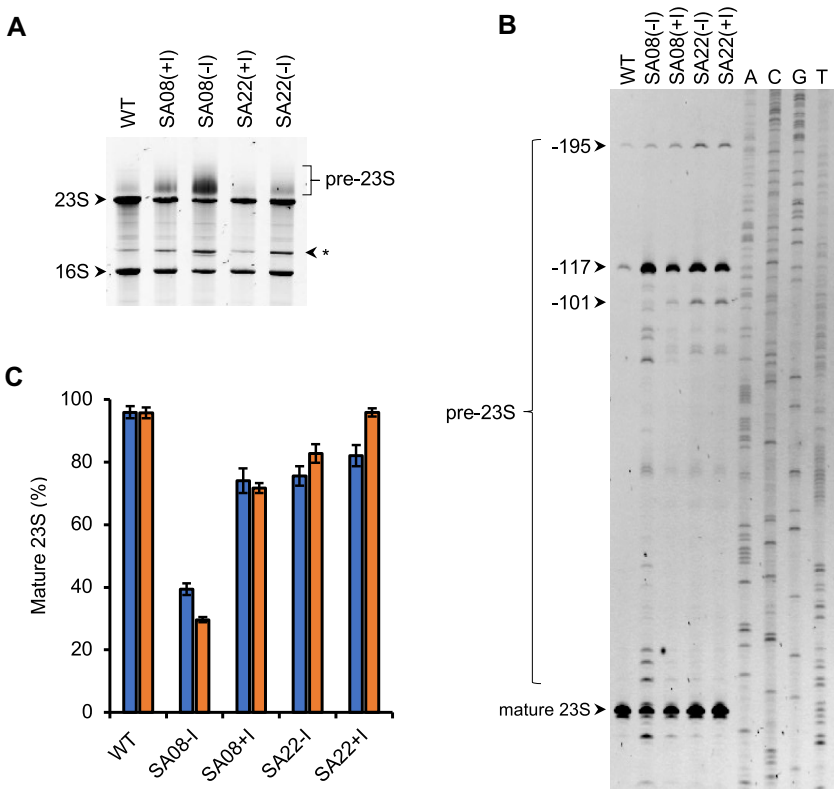

Figure 4. Depletion of bL38 inhibits processing of 23S rRNA. (**A**) A representative 4% PAGE gel, stained with SYBR Gold, showing total RNA isolated from WT, SA08, and SA22 cells grown in the presence (+I) or absence (-I) of IPTG, as indicated. Bands corresponding to 23S, 16S, and pre-23S rRNA are indicated; the asterisk marks a band of unknown origin. (**B**) Total RNA from the various strains (as indicated) was also subjected to primer extension analysis to evaluate 5′ end processing of 23S rRNA. The same primer was used to sequence plasmid-borne *rrnA*, and reactions were run in adjacent lanes (A, C, G, T). (**C**) Levels of 23S rRNA maturation, based on primer extension (blue bars) and denaturing PAGE (orange bars). Data represent mean ± SEM ($n = 3$).

the body is formed, but densities for rRNA helices H61 to H67 and r-proteins uL2, uL14, and bL19 of the interface side of the body are absent (Fig. 6). Density for the CP is also absent, as are densities for the r-protein bL9 and bL28 and rRNA helices forming the base (H73-H75) of the uL1 stalk, as well as the uL1 (H76-H78) and bL12 (H42-H44) stalks themselves. Helices forming the A (H38, H89 and H91-92), P (H69, H71, H93), and E (H68) functional sites are also invisible in the cryo-EM map. Class 2 represented 22% of the population. Compared to class 1, particles of class 2 are more mature, as rRNA helices and proteins uL2, uL14 and bL19 of the interface side of the body are visible. However, class 2 particles still lack all r-proteins and rRNA helices of the CP; bL9, bL28 and the rRNA helices forming the base of the uL1 stalk; the uL1 and bL12 stalks; and the A, P, and E functional sites. Class 3 represented 22% of the population. This map exhibits the same structural motifs seen in class 2, as well as additional density for bL9, bL28, and rRNA helices forming the base of the uL1 stalk. Partial density is also seen for H91-H92 in the A site and H93 in the P site. Class 4 represented 10% of the population. These particles contain a partially formed CP. Densities for 5S rRNA and H80-H88 of 23S rRNA are generally well defined but fragmented in some areas. Most r-proteins of the CP do not have a representative density on this map. Class 5 represented 8% of the population. These particles show fully defined rRNA components of the CP. Yet, density is lacking for r-proteins of the CP except for uL18 and bL33. Interestingly, an additional density in the E site is observed, corresponding to the GTPase Der (also known as EngA) [28, 29]. H68 adopts an extended conformation and interacts with Der, as though the factor acts as a scaffold to help fold H68. Class 6 represented 26% of the population. Class 6 particles lack Der and contain H68 in its mature conformation. The CP is largely formed, as uL5 and bL31 at the top of CP were mostly visible. However, the bL12 stalk and surrounding structural motifs, including H38 and H89 of the A site, uL16 and bL25 above and uL36, uL6 and bL38 below the bL12 stalk are invisible. Notably, these features are absent in all classes 1–6. Finally, class M (mature) particles represented 9% of the population. In these particles, structural motifs of the mature 50S subunit are represented by densities in the cryo-EM map, except for bL38, which is completely absent, as in all previous maps. Protein uL6 exhibits a highly fragmented density in the class M map, while being invisible in class 1–6 maps (Fig. 6).

Overproduction of uL6 restores growth of bL38-depleted cells.

We hypothesized that bL38 facilitates uL6 incorporation during 50S assembly in some way. To test this, we engineered two other bL38-depletion strains, SA20 and SA22, which overproduce uL6 to different degrees (Table 1). SA20 was generated by replacing *rpmL* with *rplF* on the chromosome, hence the strain carries two copies of the uL6 gene. SA22 is identical to SA20 but has another copy of *rplF* on the covering plasmid, hence the strain carries multiple copies of *rplF*.

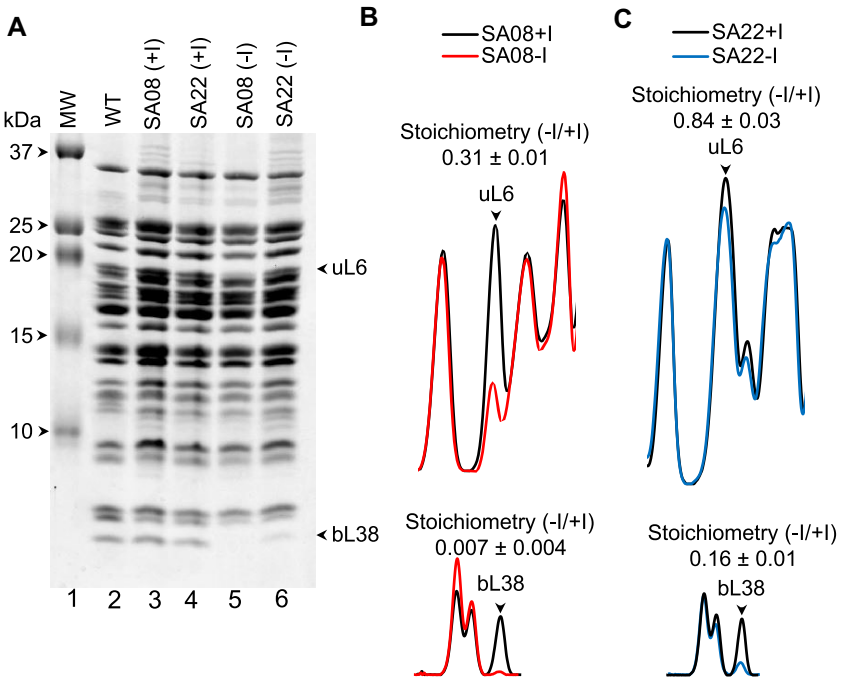

Figure 5. Protein uL6 is underrepresented in 50S particles formed in the absence of bL38. (**A**) An example SDS-PAGE experiment comparing the proteins of purified 50S subunits of wildtype *F. johnsoniae* (WT) to the proteins of 50S particles isolated from SA08 and SA22 cells grown with (+I) or without (-I) IPTG (as indicated). Bands corresponding to uL6 and bL38, verified by LC/MS-MS, are indicated. MW, molecular weight marker. (**B–C**) Examples of densitometry scans of SDS-PAGE lanes, used to quantify uL6 and bL38 in 50S particles of various cells, as indicated. Peaks corresponding to uL6 and bL38 bands are marked. Values report stoichiometry relative to the control (-IPTG/+IPTG) and correspond to the mean ± SEM ($n = 3$).

Unlike SA08, strains SA20 and SA22 grew in the absence of IPTG (Fig. 2, Table 1). Cell suspensions yielded equivalent numbers of colonies on solid media containing or lacking IPTG, although colony size was reduced for SA22 and much reduced for SA20 in the absence of IPTG. In liquid culture, SA20 and SA22 grew at rates of 0.38 and 0.56 doublings per hour, respectively, in the absence of IPTG. Under the same conditions, SA08 grew poorly, and long-term incubation led to suppressors (presumably due to mutations in *lacI*), complicating efforts to quantify growth rate (Supplementary Fig. S5). Very similar behavior was seen for ZAM66, an analogous bS21-depletion strain [9]. In the presence of IPTG, strains SA08, SA20, and SA22 grew similarly, at a rate of ~0.8 doublings per hour (Fig. 2, Table 1). These data suggest that overproduction of uL6 can compensate for the absence of bL38, with higher levels of uL6 in SA22 restoring growth to a larger degree.

Overproduction of uL6 rescues the defects caused by bL38 depletion

Strain SA22 was further characterized with respect to ribosome biogenesis. Sedimentation analysis showed similar levels of polysomes, 70S ribosomes, and subunits in cells grown without IPTG versus cells grown with IPTG (Supplementary Fig. S6). The degree of pre-23S rRNA processing was also similar with and without IPTG, based on total RNA and primer extension analyses, and clearly enhanced relative to SA08 (Fig. 4). SDS-PAGE analysis revealed that levels of uL6 are nearly equivalent in 50S particles from cells growth with or without IPTG, whereas the level of bL38 remains quite low in the latter case (Fig. 5). These findings are corroborated by LFQ analysis, which showed near-identical protein compositions of 50S(-IPTG) and 50S(+IPTG) particles with one clear exception, bL38 (Supplementary Fig. S7A). 70S ribosomes and polysomes show similar data, with underrepresentation of bL38 only in the minus IPTG case (Supplementary Fig. S7B and C). Collectively, these data suggest that overexpression of uL6 can bypass the need for bL38, restoring ribosome biogenesis and cell growth.

Cryo-EM analysis of 50S particles from strain SA22

To better understand how the overproduction of uL6 restores ribosome biogenesis in the absence of bL38, we collected 50S particles from SA22 cells grown without IPTG and analyzed them by cryo-EM. Using image classification approaches like those implemented above, we found eleven different structural classes in addition to mature subunits (Fig. 7). The cryo-EM maps representing these classes refined to resolutions ranging from 2.7 to 4 Å (Supplementary Figs S8 and S9; Supplementary Table S3). In this dataset, the most abundant subpopulation corresponded to the mature (class M) 50S subunit (26%), unlike in the SA08 case (9%, class M). Overall, the particle distribution was shifted towards classes representing later stages of assembly. For example, 83% of the particles in the SA22 case exhibited density for the CP, compared to 53% in the SA08 case. Protein uL6 was seen in four classes (7, 8, 10, M), while bL38 was absent in all classes.

The smallest assembly intermediates (classes 1 to 3) lacked the CP and showed progressive assembly of the body (Fig. 7). These intermediates closely resembled classes 1–3 of strain SA08. The other intermediates from SA22 (classes 4 to 11) were larger and showed density for at least part of the CP. Classes 4–6 of SA22 generally resembled classes 4–6 of SA08, although the degree of maturation for class 6 seems higher

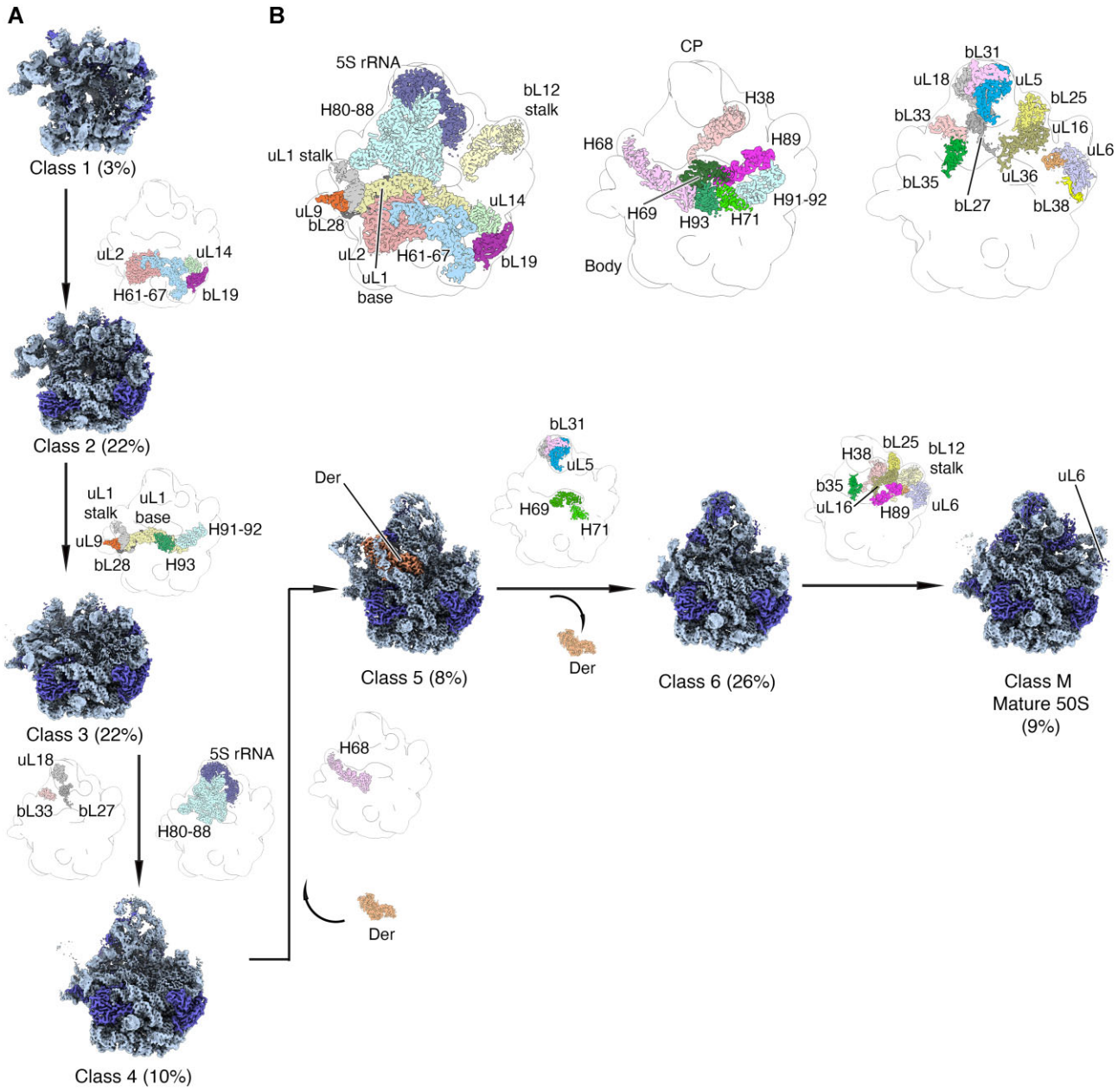

Figure 6. Assembly of the 50S subunit in the absence of bL38. (**A**) Cryo-EM maps representing the assembly intermediates of SA08(-IPTG) cells. Intermediates (classes 1–6) are arranged by increasing complexity in a potential kinetic pathway. Whether each class corresponds to an on-path intermediate remains unclear. The rRNA is shown in light steel blue and the r-proteins in slate blue. The percentages in parentheses indicate the proportion that each class represents within the population. (**B**) Diagram of the 50S subunit showing all structural elements missing from class 1. For clarity the elements are distributed onto three separate images. Color-coding of these structural elements is the same as in panel A for the small diagrams along the arrows that depict which structural elements become visible from one class to the next. Two separate small diagrams are shown for clarity in transitions where overlapping structural motifs become visible (e.g. transition from classes 3 to 4).

in the former case. An additional five intermediates (classes 7–11) were observed for SA22. While similar in size, each of these intermediates contains a unique set of r-proteins and/or folded rRNA features. Comparison of these structures suggests a complex 50S assembly landscape, with multiple parallel pathways, reminiscent of structural studies of ribosome assembly in *E. coli* and *B. subtilis* [30–34]. Three intermediates (classes 7, 8, 10) contain uL6, and these intermediates appear to be part of at least four independent paths of subunit assembly. Der is seen in two intermediates (classes 5, 7), one of which contains uL6. Overall, these results suggest that overproduction of uL6 restores a robust network of pathways of subunit formation in the absence of bL38 (Fig. 7).

Pre-50S particles from strain SA22 are bound by ribosome silencing factor RsfS

An additional density was attached to uL14 in the cryo-EM maps of various SA22 intermediates. Given the location and appearance of the density, we hypothesized that this density represented the Ribosome silencing factor (RsfS) (Supplementary Fig. S10). In *Staphylococcus aureus*, RsfS binds to uL14, preventing the association of the 50S sub-

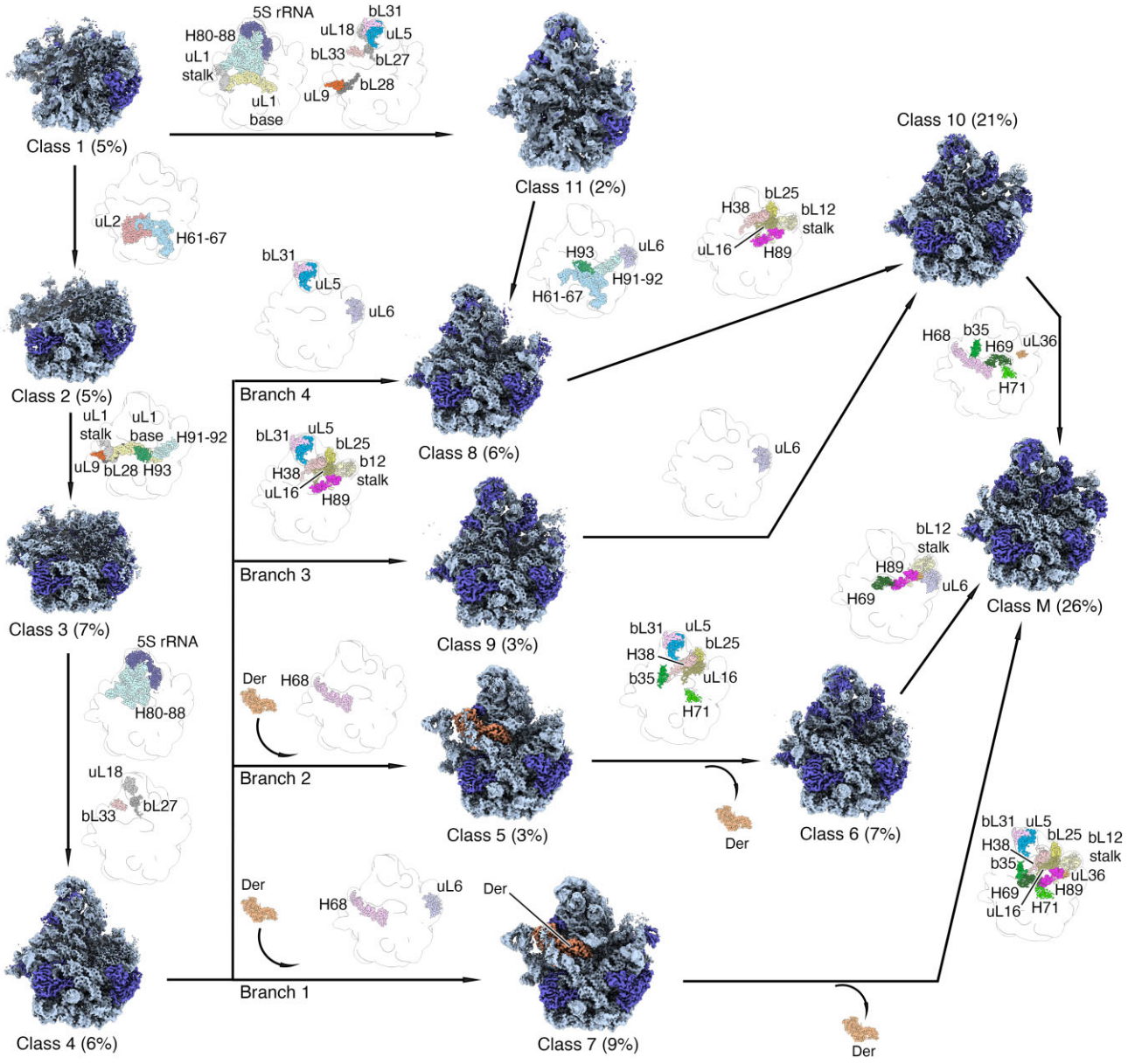

Figure 7. Assembly of the 50S subunit without bL38 but with excess uL6. Shown are cryo-EM maps that represents 50S assembly intermediates of SA22(-IPTG) cells. The maps are arranged by increasing complexity and depict multiple parallel pathways to the mature state. Whether each class corresponds to an on-path intermediate remains unclear. Diagrams between classes indicate structural elements that become visible in each inferred step, color-coded as in Fig. 6. The percentages indicate the proportion that each class represents within the population.

unit with the small subunit and tuning down translation when cells encounter stress or reach stationary phase [35]. Mitochondria and chloroplast contain RsfS homologs called C7orf30/MALSU1 and Iojap, respectively [36]. However, in these organelles, the factor seems mainly involved in ribosome biogenesis [37, 38]. Evidence that RsfS participates in ribosome biogenesis in bacteria comes from a cryo-EM study where an *in vivo* assembled 50S assembly intermediate contained RsfS and three other assembly factors (YjgA, RluD and ObgE) [39].

In the absence of a molecular model of *F. johnsoniae* RsfS, we obtained the AlphaFold predicted structure (https://alphafold.ebi.ac.uk/entry/A5FGN5) and docked the model into the additional density of the cryo-EM maps of the assembly intermediates from SA22 cells (Supplementary Fig. S10C). The best docking position for the AlphaFold model closely matched the position and orientation of the experimental cryo-EM structure of the RsfS-50S complex from *S. aureus* [35], suggesting that this additional density represents the RsfS protein. Consistent with the study in *S. aureus* [35] and *E. coli* [39], the RsfS protein also contacts uL14 (Supplementary Fig. S10). Our finding that RsfS was bound to most 50S intermediates purified from SA22 cells represents additional evidence that this factor also plays a role during ribosome biogenesis in bacteria and probably prevents premature association of the ribosomal subunits before the assembly process is completed. A density representing RsfS was not observed in any of the seven assembly intermediates accumulating in the SA08(-IPTG) cells, even though classes 1–6 and M look otherwise similar.

Visualization of helix H1 of the pre-23S rRNA

In *E. coli*, the 5′ and 3′ ends of mature 23S rRNA form an 8 bp helix termed H1, which is the remnant of a much larger leader-trailer helix of pre-23S rRNA. In *F. johnsoniae*, H1 exists as part of the leader-trailer structure and is completely removed during subunit maturation [40]. Given the incomplete processing of the 23S rRNA in SA08(-IPTG) cells (Fig. 4), we looked for evidence of H1 in the cryo-EM maps of pre-50S intermediates. Indeed, all intermediates showed unassigned density in the shape of an RNA helix near the position of the 5′ and 3′ ends of 23S rRNA in the mature subunit (Fig. 8, Supplementary Fig. S11). Nucleotides of the proximal leader (5′-CAAUAAGCA-3′) and trailer (5′-UAAGCUUAUGU-3′) were readily modeled into the density, revealing seven base pairs of H1. Compared to its position in the mature subunit, the 5′ end of 23S rRNA is flipped by ∼180 degrees to enable H1 formation, as predicted previously [40]. Densities for H1 were also seen in the 12 classes of particles from SA22(-IPTG) cells (Supplementary Fig. S12). However, this density was fragmented, particularly in more mature particles, consistent with a substantial degree of end maturation (Fig. 4C). These results provide structural evidence that 50S assembly intermediates of SA08 and SA22 cells contain leader and trailer sequences, which form a panhandle helix (H1) that extends beyond the solvent surface of the 50S subunit. The single strands that link H1 to 23S rRNA look accessible to the RNase(s) needed to finish rRNA processing.

Cryo-EM analysis of translating ribosomes from strain SA22

To determine if ribosomes assembled in the absence of bL38 and presence of excess uL6 had any structural defects, 70S and polysome particles from SA22(-IPTG) cells were deposited into cryo-EM grids and imaged in the electron microscope. Image classification approaches showed that ribosomes assembled under these conditions exhibited no obvious defects. Some contained tRNA molecules, indicating they were engaged in translation (Supplementary Fig. S13). Particles from the 70S peak fell into four classes (Supplementary Fig. S13A). The most abundant was class 1, which accounted for 47% of the particles and represented empty ribosomes with no tRNA molecules bound. Class 2 represented 36% of the particles and contained a tRNA molecule in the classical P/P site. The least abundant classes were 3 and 4, attracting 14% and 3% of the particles, respectively. Class 3 contained two tRNA molecules—one in the A/A site and one in the P/P site. Class 4 ribosomes had one tRNA molecule in the hybrid P/E site. Particles in the polysome peak fell into five classes (Supplementary Fig. S13B). Overall, the percentage of ribosomes with bound tRNA was higher in the polysome sample (78%, versus 53% in the 70S sample), indicating a larger proportion of ribosomes engaged in translation. Class 1 particles (22%) were vacant. Class 2 particles (40%) had one tRNA molecule in the P/P site. Class 3 particles (11%) contained tRNA molecules in the A/A and P/P sites. Class 4 particles (15%) had tRNA molecules in the A/A and P/E sites. Finally, class 5 particles (12%) contained one tRNA molecule in the P/E site. The cryo-EM maps representing these nine different classes from the two samples refined to resolutions ranging from 2.7 to 4.2 Å (Supplementary Figs S14–S17; Supplementary Tables S4–S5). The presence of uL6 was evident in all classes, but in no class was density for bL38 seen. These results suggest that overproduction of uL6 enables assembly of ribosomes in the absence of bL38, and these ribosomes are active.

Strains of F. johnsoniae that completely lack bL38

It remained unclear whether a small amount of bL38 might be produced in SA08 and SA22 cells grown in the absence of IPTG. To address this ambiguity, we attempted to replace *rpmL* on the chromosome with *rplF* in the absence and presence of a plasmid harboring another copy of *rplF*. Success was found in both cases, resulting in strains SA28 and SA30. Neither of these strains contains *rpmL*, unequivocally showing that bL38 is dispensable when uL6 is overproduced. The growth of all strains was measured in parallel (Table 1) in the absence of tetracycline (Tet), an antibiotic included previously for transformed strains. Growth of SA08, SA20, and SA22 was generally faster without Tet, even though these strains carry plasmid-borne *tetQ* [12]. Regardless, the trend of growth rates (SA08 < SA20 < SA22) in the absence of IPTG remained the same. Importantly, SA28 grew virtually as fast as SA20, and SA30 grew nearly as fast as SA22 (Table 1). These data suggest little-to-no leaky expression of plasmid-borne *rpmL* in SA08 or SA22 without inducer. Unlike SA08 and SA22, strains SA28 and SA30 could be cultured repeatedly with no evidence of suppressor mutations and thus appear to be genetically stable (Supplementary Fig. S18). Collectively, these data confirm that elevated levels of uL6 can bypass the need for bL38.

F. johnsoniae uL6 is stabilized by bL38 off the ribosome

Why bL38 is needed in the Bacteroidia but absent from other bacteria remained unclear. We hypothesized that uL6 is labile in the Bacteroidia, due to intrinsic properties of the protein or cytoplasmic proteases, and bL38 stabilizes and/or protects uL6 in the cell. To test this, we purified *F. johnsoniae* uL6, *E. coli* uL6, and *F. johnsoniae* bL38 and studied their properties and interactions using DSF (Fig. 9, Supplementary Fig. S19). DSF relies on an environmentally sensitive dye (e.g. SYPRO Orange) to monitor protein unfolding as a function of temperature [41, 42]. Interaction of the dye with hydrophobic residues, exposed during protein denaturation, can cause an increase in fluorescence signal. *E. coli* uL6 showed a typical DSF profile, with SYPRO Orange fluorescence intensity increasing from ∼30°C to 55°C (maximum), and then decreasing at higher temperatures, presumably due to protein aggregation (Fig. 9B, top). A secondary plot of the first derivative values enables estimation of the melting temperature (T_m), 44 ± 1°C, for *E. coli* uL6, under these conditions (Fig. 9B, bottom). *F. johnsoniae* uL6 gave a similarly-shaped DSF curve, albeit shifted substantially to the left, corresponding to $T_m = 27 \pm 1$°C. Thus, *F. johnsoniae* uL6 is intrinsically less stable than *E. coli* uL6. Protein bL38, even at high concentration (60 μM; Supplementary Fig. S19C), showed virtually no effect on SYPRO Orange fluorescence across the same range of temperatures. Similar results have been seen for other proteins and have been attributed to the idiosyncratic nature of dye-protein interactions [43]. Importantly, when bL38 (10 μM) was added to the same concentration of *F. johnsoniae* uL6, the DSF curve shifted rightward, increasing the T_m to 34°C (Fig. 9B). Higher concentrations of bL38 increased the T_m further, to 39°C, 12 degrees higher than in the absence of bL38 (Fig. 9C, Supplementary Fig. S19A). Addition of bL38 to *E. coli*

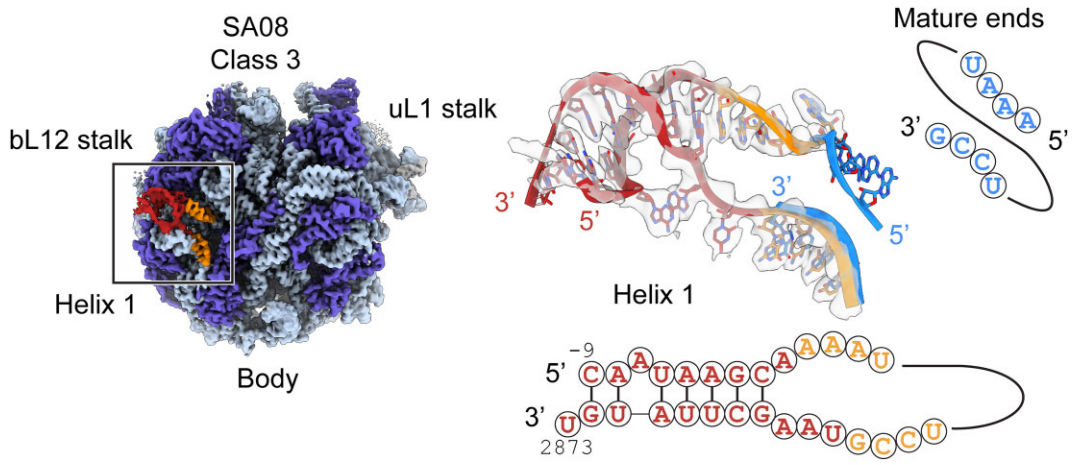

Figure 8. Visualization of helix H1 of the precursor leader and trailer sequences. Solvent view of the cryo-EM map obtained for the class 3 intermediate of SA08(-IPTG) cells (left image). Main landmarks of the ribosomal particle are labeled. The r-proteins are colored in slate blue and the rRNA is shown in light steel blue. The 5′ and 3′ ends of 23S rRNA (orange) and precursor sequences forming helix H1 (brick red) are highlighted. Shown on the right is semi-transparent density into which the precursor rRNA sequences have been fitted. The conformation adopted by the 5′ and 3′ ends of 23S in these assembly intermediates is shown in orange. The conformation of the 5′ and 3′ ends in the mature 50S subunit is different and shown by the overlapping molecular model in cyan. Corresponding sequences of the pre-23S rRNA and mature 23S rRNA are also shown, with the same color coding.

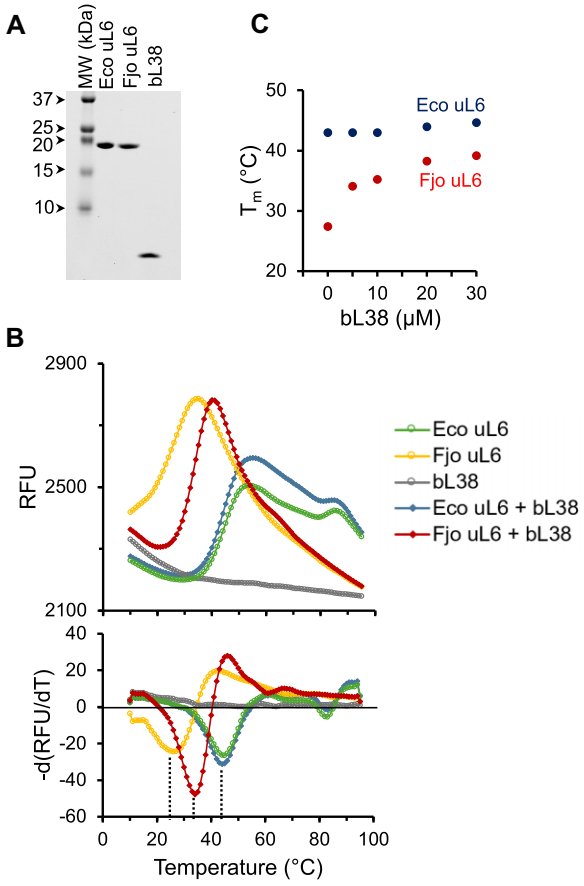

Figure 9. Effect of bL38 on uL6 stability. (**A**) Tricine urea SDS-PAGE gel showing purified uL6 of *E. coli* (Eco), uL6 of *F. johnsoniae* (Fjo), and bL38 of *F. johnsoniae*, as indicated. (**B**) DSF of individual and combined proteins, as indicated in the key. RFU, relative fluorescence units. Primary data are shown in the top panel and corresponding secondary (first-derivative) plots are shown in the bottom panel. Minima in the secondary plots indicate melting temperature (T_m) values, exemplified by the dashed lines. (**C**) T_m values for *E. coli* uL6 (dark blue) and *F. johnsoniae* uL6 (red) are plotted as a function of bL38 concentration.

uL6 had no such effect (Fig. 9C, Supplementary Fig. S19B), indicating that the stabilizing interaction is specific to the *F. johnsoniae* protein pair. Collectively, these data suggest that bL38 binds and stabilizes uL6 off the ribosome in the Bacteroidia.

Discussion

In this work, we show that bL38 plays a critical role in 50S biogenesis in *F. johnsoniae*. Depletion of bL38 arrests cell growth and causes accumulation of pre-50S particles, which are unable to enter the translationally-active pool. These particles lack bL38, have reduced levels of uL6 and uL10, and retain pre-23S leader and trailer sequences. Cryo-EM analysis reveals an absence of density for uL6 and entire bL12 stalk region, and additional density corresponding to the unprocessed ends of 23S rRNA. Strikingly, overproduction of uL6 partially rescues all the phenotypes of the bL38 depletion strain. A strain carrying two copies of *rplF* (uL6) can live without *rpmL* (bL38), and introduction of another plasmid-borne copy of *rplF* enables quite robust growth. These findings strongly suggest that bL38 facilitates uL6 incorporation during 50S assembly in the Bacteroidia.

Protein bL38 interacts intimately with uL6 on the ribosome, with nearly 40% of bL38's surface area buried by uL6. Our DSF data show that bL38 also interacts with uL6 off the ribosome, stabilizing uL6 substantially. We propose that bL38 and uL6 heterodimerize in the cytoplasm and then become incorporated into the maturing subunit during 50S biogenesis. In this way, bL38 would be effectively acting as a chaperone to facilitate uL6 incorporation and/or prevent its degradation. This model is fully in line with our genetic data. Overproduction of uL6 could circumvent the need for bL38 by (i) generating sufficient folded (active) protein, (ii) promoting the incorporation of uL6 by mass action, and/or (iii) overwhelming proteases that would otherwise degrade uL6 in the absence of bL38.

Protein uL6 of *F. johnsoniae* is intrinsically unstable, exhibiting a melting temperature of 27°C, three degrees below

the optimum temperature of cell growth (30°C). Protein bL38 increases the T_m of uL6 to 39°C, five degrees higher than the maximal temperature of cell growth (34°C). An alignment of uL6 sequences from representative bacteria across the phylogenetic tree is shown in Supplementary Fig. S20A. Intriguingly, an insertion of four residues in loop 11 (between β10 and β11) of the protein is seen in representatives of class Bacteroidia and class Rhodothermia (*R. marinus*) but absent in representatives of other lineages, a distribution reflecting that of the bL38 gene (DUF4295) [6]. This four-residue insertion lies in the C-terminal domain but does not contribute to the binding site of bL38 (Fig. 1, Supplementary Fig. S20B). It is possible that the extended loop 11 of Bacteroidia uL6 contributes to the protein's lability, which is allosterically countered by the binding of bL38. Future work will be needed to test this idea and further understand the thermodynamics of uL6 and bL38.

Cryo-EM analysis of 50S particles from SA08 and SA22 cells reveals assembly intermediates at various stages of maturation. By comparing the structures obtained, we can infer potential kinetic pathways of assembly in the two cases. In the SA08(-IPTG) case, six intermediates were observed, and these can be arranged on a progressive linear path toward assembly (Fig. 6). All six intermediates lack uL6, and the last deduced step (to class M) involves incorporation of several r-proteins (uL6, uL16, bL25, bL35, and uL36) and folding of various rRNA elements (H42-H44, H89, and H38). In the SA22(-IPTG) case, nearly twice as many intermediates were observed, and five parallel pathways can be inferred (Fig. 7). This suggests a broader kinetic landscape and more robust process when uL6 incorporation can occur. Class 8 and class 10 intermediates contain uL6, and three of the five parallel paths include one or both of those intermediates. One would predict that without uL6 incorporation these paths would be blocked, resulting in a narrowed kinetic landscape like that of Fig. 6.

Nearly all 50S assembly intermediates from SA22 showed clear density for RsfS, bound to uL14. As these intermediates were isolated from exponential-phase cells grown under optimal conditions, these data provide strong evidence that RsfS normally contributes to 50S biogenesis, in line with other recent work [39]. Intermediates from SA08 did not show density for RsfS, even though uL14 was present in most particles (97%). However, we suspect this stems from lower stoichiometry of RsfS in the SA08 case (0.21 ± 0.04) compared to the SA22 case (0.57 ± 0.07), as estimated by LFQ. Pre-50S particles accumulate to high levels in SA08(-IPTG) cells, and there simply may not be enough RsfS to bind all the existing assembly intermediates.

As part of this study, we mapped the 5′ ends of pre-23S rRNA intermediates of *F. johnsoniae* to positions −195, −117, and −100 (Supplementary Fig. S1). Position -195 lies just downstream from $tRNA^{Ala}$, and cleavage at this site is predicted to generate a $tRNA^{Ala}$ precursor without C75 and A76 (tRNA numbering). The critical 3′ CCA end of this tRNA, and many others in *F. johnsoniae*, is not genomically encoded and presumably added post-transcriptionally by tRNA nucleotidyl transferase. Position −117 lies near the base of the leader-trailer helix (HLT), while position -100 lies near the center of HLT. Little is known about rRNA processing in the Bacteroidia. The genome of *F. johnsoniae* encodes various ribonucleases, including RNase E/G and RNase III; however, which enzymes are responsible for these processing events remains to be determined.

Recently, a cryo-EM structure of the hibernating 70S ribosome from *Borreliella burgdorferi*, a member of Spirochaetota, was determined at 2.9 Å resolution [44]. A small protein, interacting with uL6, was identified as bL38. *B. burgdorferi* bL38 and *F. johnsoniae* bL38 share 18.2% sequence identity and 43.6% similarity (based on GGsearch2SEQ), values considerably lower than those of other ribosomal proteins, including uL6 (48.4% identical / 75.5% similar). Obvious structural differences between the two proteins exist as well. *B. burgdorferi* bL38 includes an additional beta strand (β3) and its short alpha helix is oriented in the opposite direction and packed against the opposite face of the β1-β2 hairpin, compared to *F. johnsoniae* bL38. Moreover, the entire protein is shifted toward uL14 and bL19 in the *B. burgdorferi* ribosome, by ∼10 Å [44]. These observations raise the question of whether *B. burgdorferi* bL38 and *F. johnsoniae* bL38 are truly homologous. However, bL38 from *Rhodothermus marinus* appears to be homologous to both *B. burgdorferi* bL38 (24.6% identity; 57.9% similarity) and *F. johnsoniae* bL38 (27.8% identity; 57.4% similarity), suggesting that all three proteins share a common ancestor (Supplementary Fig. S21). The high degree of sequence/structural diversity of the bL38 protein implies considerable plasticity in the bL38–uL6 interface. Further work will be needed to clarify which bacterial clades rely on bL38 and whether all bL38 proteins function in the same way.

Acknowledgements

We thank Z. A. McNutt, B. Roy, and B. Warner for technical assistance; K-M. Moon for sample handling and preparation advice; B. R. Warner and T. Magliery for helpful discussions; and staff of the Facility for Electron Microscopy Research (FEMR) at McGill University for support on cryo-EM data collection.

Author contributions: Conceptualization, K.F. and M.S.A; Investigation, M.S.A., D.A., H.Z., and B.N.H.; Resources and Supervision, K.F., J.O., and L.J.F.; Writing—original draft, K.F., M.S.A., and J.O.; Writing—review & editing, all authors.

Supplementary data

Supplementary data is available at NAR online.

Conflict of interest

None declared.

Funding

This work was supported by grants from the National Science Foundation (MCB-2029502 and MCB-2344534 to K.F.), National Institutes of Health (GM072528 to K.F.), and NSERC Discovery Program (RGPIN-2019-05799 to J.O.). BH was supported by a 4YF from the University of British Columbia. Work in L.J.F.'s group was supported by the Canada Foundation for Innovation, the BC Knowledge Development Fund, and Genome BC (374PRO). Cryo-EM data was collected at the Facility for Electron Microscopy Research (FEMR)

at McGill. FEMR is supported by the Canadian Foundation for Innovation, Quebec Government and McGill University. Funding to pay the Open Access publication charges for this article was provided by National Science Foundation.

Data availability

The cryo-EM maps obtained in this study have been deposited in the Electron Microscopy Data Bank (EMDB), and the accession codes are detailed in Supplementary Tables S2-S25. The proteomics data have been deposited to the ProteomeXchange Consortium via the PRIDE [19] partner repository with the dataset identifier PXD050205.

References

1. Ban N, Beckmann R, Cate JH *et al.* A new system for naming ribosomal proteins. *Nat Commun* 2014;**24**:1439–50. https://doi.org/10.1016/j.sbi.2014.01.002
2. Yutin N, Puigbo P, Koonin EV *et al.* Phylogenomics of prokaryotic ribosomal proteins. *PLoS One* 2012;**7**:e36972. https://doi.org/10.1371/journal.pone.0036972
3. Brodersen DE, Clemons WM Jr, Carter AP *et al.* Crystal structure of the 30 S ribosomal subunit from Thermus thermophilus: structure of the proteins and their interactions with 16 S RNA. *J Mol Biol* 2002;**316**:725–68. https://doi.org/10.1006/jmbi.2001.5359
4. Hentschel J, Burnside C, Mignot I *et al.* The complete structure of the mycobacterium smegmatis 70S ribosome. *Cell Rep* 2017;**20**:149–60. https://doi.org/10.1016/j.celrep.2017.06.029
5. Li Z, Ge X, Zhang Y *et al.* Cryo-EM structure of mycobacterium smegmatis ribosome reveals two unidentified ribosomal proteins close to the functional centers. *Protein Cell* 2018;**9**:384–8.
6. Jha V, Roy B, Jahagirdar D *et al.* Structural basis of sequestration of the anti-shine-dalgarno sequence in the Bacteroidetes ribosome. *Nucleic Acids Res* 2021;**49**:547–67. https://doi.org/10.1093/nar/gkaa1195
7. Baez WD, Roy B, McNutt ZA *et al.* Global analysis of protein synthesis in Flavobacterium johnsoniae reveals the use of Kozak-like sequences in diverse bacteria. *Nucleic Acids Res* 2019;**47**:10477–88. https://doi.org/10.1093/nar/gkz855
8. McBride MJ, Xie G, Martens EC *et al.* Novel features of the polysaccharide-digesting gliding bacterium Flavobacterium johnsoniae as revealed by genome sequence analysis. *Appl Environ Microb* 2009;**75**:6864–75. https://doi.org/10.1128/AEM.01495-09
9. McNutt ZA, Roy B, Gemler BT *et al.* Ribosomes lacking bS21 gain function to regulate protein synthesis in Flavobacterium johnsoniae. *Nucleic Acids Res* 2023;**51**:1927–42. https://doi.org/10.1093/nar/gkad047
10. Gibson DG, Young L, Chuang RY *et al.* Enzymatic assembly of DNA molecules up to several hundred kilobases. *Nat Methods* 2009;**6**:343–5. https://doi.org/10.1038/nmeth.1318
11. Zhu Y, Thomas F, Larocque R *et al.* Genetic analyses unravel the crucial role of a horizontally acquired alginate lyase for brown algal biomass degradation by Zobellia galactanivorans. *Environ Microbiol* 2017;**19**:2164–81. https://doi.org/10.1111/1462-2920.13699
12. Agarwal S, Hunnicutt DW, McBride MJ. Cloning and characterization of the Flavobacterium johnsoniae (Cytophaga johnsonae) gliding motility gene, gldA. *Proc Natl Acad Sci USA* 1997;**94**:12139–44. https://doi.org/10.1073/pnas.94.22.12139
13. McBride MJ, Kempf MJ. Development of techniques for the genetic manipulation of the gliding bacterium cytophaga johnsonae. *J Bacteriol* 1996;**178**:583–90. https://doi.org/10.1128/jb.178.3.583-590.1996
14. Qin D, Fredrick K. Analysis of polysomes from bacteria. *Methods Enzymol* 2013;**530**:159–72. https://doi.org/10.1016/B978-0-12-420037-1.00008-7
15. McNutt ZA, Gandhi MD, Shatoff EA *et al.* Comparative analysis of anti-shine- dalgarno function in Flavobacterium johnsoniae and Escherichia coli. *Front Mol Biosci* 2021;**8**:787388. https://doi.org/10.3389/fmolb.2021.787388
16. Schagger H, von Jagow G. Tricine-sodium dodecyl sulfate-polyacrylamide gel electrophoresis for the separation of proteins in the range from 1 to 100 kDa. *Anal Biochem* 1987;**166**:368–79. https://doi.org/10.1016/0003-2697(87)90587-2
17. Shevchenko A, Wilm M, Vorm O *et al.* Mass spectrometric sequencing of proteins silver-stained polyacrylamide gels. *Anal Chem* 1996;**68**:850–8. https://doi.org/10.1021/ac950914h
18. Rappsilber J, Ishihama Y, Mann M. Stop and go extraction tips for matrix-assisted laser desorption/ionization, nanoelectrospray, and LC/MS sample pretreatment in proteomics. *Anal Chem* 2003;**75**:663–70. https://doi.org/10.1021/ac026117i
19. Perez-Riverol Y, Bai J, Bandla C *et al.* The PRIDE database resources in 2022: a hub for mass spectrometry-based proteomics evidences. *Nucleic Acids Res* 2022;**50**:D543–52. https://doi.org/10.1093/nar/gkab1038
20. Schorb M, Haberbosch I, Hagen WJH *et al.* Software tools for automated transmission electron microscopy. *Nat Methods* 2019;**16**:471–7. https://doi.org/10.1038/s41592-019-0396-9
21. Punjani A, Rubinstein JL, Fleet DJ *et al.* cryoSPARC: algorithms for rapid unsupervised cryo-EM structure determination. *Nat Methods* 2017;**14**:290–6. https://doi.org/10.1038/nmeth.4169
22. Pettersen EF, Goddard TD, Huang CC *et al.* UCSF Chimera–a visualization system for exploratory research and analysis. *J Comput Chem* 2004;**25**:1605–12. https://doi.org/10.1002/jcc.20084
23. Pettersen EF, Goddard TD, Huang CC *et al.* UCSF ChimeraX: structure visualization for researchers, educators, and developers. *Protein Sci* 2021;**30**:70–82. https://doi.org/10.1002/pro.3943
24. Henderson R, Sali A, Baker ML *et al.* Outcome of the first electron microscopy validation task force meeting. *Structure* 2012;**20**:205–14. https://doi.org/10.1016/j.str.2011.12.014
25. Choudhary D, Kumar A, Magliery TJ *et al.* Using thermal scanning assays to test protein-protein interactions of inner-ear cadherins. *PLoS One* 2017;**12**:e0189546. https://doi.org/10.1371/journal.pone.0189546
26. Huynh K, Partch CL. Analysis of protein stability and ligand interactions by thermal shift assay. *Curr Protoc Protein Sci* 2015;**79**:28.9.1–14. https://doi.org/10.1002/0471140864.ps2809s79
27. Naganathan A, Culver GM. Interdependency and redundancy add complexity and resilience to biogenesis of bacterial ribosomes. *Annu Rev Microbiol* 2022;**76**:193–210. https://doi.org/10.1146/annurev-micro-041020-121806
28. Zhang X, Yan K, Zhang Y *et al.* Structural insights into the function of a unique tandem GTPase EngA in bacterial ribosome assembly. *Nucleic Acids Res* 2014;**42**:13430–9. https://doi.org/10.1093/nar/gku1135
29. Arpin D, Palacios A, Basu K *et al.* The binding of RbgA to a critical 50S assembly intermediate facilitates YphC function in bacterial ribosomal assembly. *Nucleic Acids Res* 2024
30. Davis JH, Tan YZ, Carragher B *et al.* Modular assembly of the bacterial large ribosomal subunit. *Cell* 2016;**167**:1610–22. https://doi.org/10.1016/j.cell.2016.11.020
31. Qin B, Lauer SM, Balke A *et al.* Cryo-EM captures early ribosome assembly in action. *Nat Commun* 2023;**14**:898. https://doi.org/10.1038/s41467-023-36607-9
32. Seffouh A, Jain N, Jahagirdar D *et al.* Structural consequences of the interaction of RbgA with a 50S ribosomal subunit assembly intermediate. *Nucleic Acids Res* 2019;**47**:10414–25. https://doi.org/10.1093/nar/gkz770

33. Seffouh A, Trahan C, Wasi T *et al.* RbgA ensures the correct timing in the maturation of the 50S subunits functional sites. *Nucleic Acids Res* 2022;**50**:10801–16. https://doi.org/10.1093/nar/gkac059
34. Sheng K, Li N, Rabuck-Gibbons JN *et al.* Assembly landscape for the bacterial large ribosomal subunit. *Nat Commun* 2023;**14**:5220. https://doi.org/10.1038/s41467-023-40859-w
35. Khusainov I, Fatkhullin B, Pellegrino S *et al.* Mechanism of ribosome shutdown by RsfS in Staphylococcus aureus revealed by integrative structural biology approach. *Nat Commun* 2020;**11**:1656. https://doi.org/10.1038/s41467-020-15517-0
36. Hauser R, Pech M, Kijek J *et al.* RsfA (YbeB) proteins are conserved ribosomal silencing factors. *PLoS Genet* 2012;**8**:e1002815. https://doi.org/10.1371/journal.pgen.1002815
37. Rorbach J, Gammage PA, Minczuk M. C7orf30 is necessary for biogenesis of the large subunit of the mitochondrial ribosome. *Nucleic Acids Res* 2012;**40**:4097–109. https://doi.org/10.1093/nar/gkr1282
38. Walbot V, Coe EH. Nuclear gene iojap conditions a programmed change to ribosome-less plastids in Zea mays. *Proc Natl Acad Sci USA* 1979;**76**:2760–4. https://doi.org/10.1073/pnas.76.6.2760
39. Nikolay R, Hilal T, Schmidt S *et al.* Snapshots of native pre-50S ribosomes reveal a biogenesis factor network and evolutionary specialization. *Mol Cell* 2021;**81**:1200–15. https://doi.org/10.1016/j.molcel.2021.02.006
40. Shatoff EA, Gemler BT, Bundschuh R *et al.* Maturation of 23S rRNA includes removal of helix H1 in many bacteria. *RNA Biol* 2021;**18**:856–65. https://doi.org/10.1080/15476286.2021.2000793
41. Layton CJ, Hellinga HW. Quantitation of protein-protein interactions by thermal stability shift analysis. *Protein Sci* 2011;**20**:1439–50. https://doi.org/10.1002/pro.674
42. Wu T, Hornsby M, Zhu L *et al.* Protocol for performing and optimizing differential scanning fluorimetry experiments. *STAR Protoc* 2023;**4**:102688. https://doi.org/10.1016/j.xpro.2023.102688
43. Wu T, Yu JC, Suresh A *et al.* Protein-adaptive differential scanning fluorimetry using conformationally responsive dyes. *Nat Biotechnol* 2024;**43**:106–13. https://doi.org/10.1038/s41587-024-02158-7
44. Sharma MR, Manjari SR, Agrawal EK *et al.* The structure of a hibernating ribosome in a Lyme disease pathogen. *Nat Commun* 2023;**14**:6961. https://doi.org/10.1038/s41467-023-42266-7

Received: March 7, 2024. **Revised:** February 4, 2025. **Editorial Decision:** February 4, 2025. **Accepted:** February 6, 2025